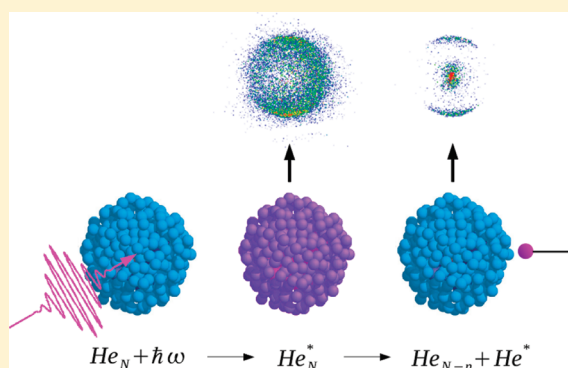


Femtosecond Photoelectron Imaging of Transient Electronic States and Rydberg Atom Emission from Electronically Excited He Droplets[†]Oleg Kornilov,^{*,‡,§} Oliver Bünermann,^{‡,||} Daniel J. Haxton,[‡] Stephen R. Leone,^{‡,⊥,¶} Daniel M. Neumark,^{‡,⊥} and Oliver Gessner[‡][†]Ultrafast X-ray Science Laboratory, Chemical Sciences Division, Lawrence Berkeley National Laboratory, Berkeley, California 94720, United States[⊥]Departments of Chemistry and [¶]Physics, University of California at Berkeley, Berkeley, California 94720, United States

ABSTRACT: Ultrafast relaxation of electronically excited pure He droplets is investigated by femtosecond time-resolved photoelectron imaging. Droplets are excited by extreme ultraviolet (EUV) pulses with photon energies below 24 eV. Excited states and relaxation products are probed by ionization with an infrared (IR) pulse with 1.6 eV photon energy. An initially excited droplet state decays on a time scale of 220 fs, leading predominantly to the emission of unaligned 1s3d Rydberg atoms. In a second relaxation channel, electronically aligned 1s4p Rydberg atoms are emitted from the droplet within less than 120 fs. The experimental results are described within a model that approximates electronically excited droplet states by localized, atomic Rydberg states perturbed by the local droplet environment in which the atom is embedded. The model suggests that, below 24 eV, EUV excitation preferentially leads to states that are localized in the surface region of the droplet. Electronically aligned 1s4p Rydberg atoms are expected to originate from excitations in the outermost surface regions, while nonaligned 1s3d Rydberg atoms emerge from a deeper surface region with higher local densities. The model is used to simulate the He droplet EUV absorption spectrum in good agreement with previously reported fluorescence excitation measurements.



1. INTRODUCTION

Helium droplets attract significant interest from many scientific communities owing to their unique properties. Their low equilibrium temperature (0.37 K¹), superfluidity,² and large pick-up cross sections make them ideal hosts for ultracold rotational, vibrational, and electronic spectroscopy of embedded species.^{3–6} In these studies, all the He atoms are in their ground state, and the interactions involving these atoms are very well described by weak van der Waals forces. In contrast, the stronger interactions in droplets in which He atoms are electronically excited lead to novel electronic and nuclear dynamics that thus far are not well understood. Electronically excited helium droplets have been studied by several groups using fluorescence emission spectroscopy,^{7–9} photoion¹⁰ and photoelectron^{11,12} spectroscopy, and electronic structure calculations.^{13,14} Most recently, time-resolved photoelectron¹⁵ and photoion¹⁶ imaging experiments using novel femtosecond EUV laser light sources have been performed. The work by Bünermann et al.¹⁶ as well as earlier experiments employing spectrally resolved fluorescence⁸ demonstrate that the relaxation dynamics of droplets excited below and above 24 eV differ dramatically. Here, we examine the dynamics induced by excitation below this critical energy by carrying out femtosecond time-resolved photoelectron spectroscopy experiments on large He droplets with $\approx 2 \times 10^6$ atoms, which are excited at extreme ultraviolet (EUV) photon energies restricted

below 24 eV. We compare our results to previous work¹⁵ in which a broader pump-photon range was used that extended significantly beyond 24 eV. A quantitative model for electronic excitations is proposed based on a picture of perturbed Rydberg states of individual atoms.

The first experimental investigation of electronic excitations in neutral He droplets was carried out by Joppien et al.⁷ who detected EUV fluorescence after excitation with synchrotron radiation. The results revealed two broad excitation bands centered at about 21.6 and 23.8 eV. A follow-up study that spectrally resolved the emitted light⁸ showed that relaxation of the droplets excited above 23 eV led to emission of Rydberg atoms and molecules with the fraction of emitted molecules increasing at larger excitation energies. At energies above 24 eV, emission from triplet states was observed, suggesting that the character of the excited states was different from those below 24 eV. Photoionization measurements by Fröchtenicht et al.¹⁰ showed that, above 23 eV, the fluorescence relaxation channel was complemented by ionization of the droplet leading to the formation of small ionic fragments (He_N^+ , $N \leq 17$) as well as very large ions ($N > 10^3$). This study suggested that, below the

Received: January 14, 2011

Revised: June 2, 2011

Published: June 20, 2011

ionization threshold of atomic He (24.59 eV), the droplets were ionized indirectly via an autoionization mechanism. This channel was further investigated by Neumark and co-workers using photoelectron imaging.^{11,12} They found that photoelectron spectra of He droplets at excitation energies below the atomic ionization potential (IP) consisted of a single peak of ultraslow electrons with average kinetic energies of less than 1 meV. These spectra were interpreted as evidence for a strong interaction of the photoelectrons with the droplet environment during the autoionization process. In contrast, the photoelectron spectrum for excitation energies above the atomic IP was dominated by direct ionization, with only a small contribution from ultraslow photoelectrons.

To gain a deeper understanding of the electronically excited droplet states and their relaxation dynamics, real-time studies have been performed using femtosecond time-resolved photoelectron and photoion imaging spectroscopy.^{15–19} This line of research has recently been enabled by the development of bright femtosecond light sources in the EUV photon energy range.^{20–22} These sources are based on high-order harmonic generation, which partially converts the energy of intense femtosecond infrared pulses to high harmonics via nonlinear interaction with gaseous media. Using this capability, He droplets were investigated in a femtosecond pump–probe experiment in which the upper band in the droplets was excited by a broad EUV pulse centered around 23.7 eV and ionized with a 785 nm probe pulse. The resulting photoelectron images yielded time-dependent electron kinetic energy and angular distributions,¹⁵ which showed evidence for time-resolved decay of the initially excited state via emission of He* Rydberg atoms and by interband relaxation to the lower droplet electronic band at 21.6 eV. Two time constants were identified. A faster 280 fs time constant was associated with an intraband relaxation within the upper electronic band, while a slower 2.8 ps time scale was attributed to the interband relaxation. The results suggested that the probe pulse re-excited population from the lower to the upper band, resulting in up to a 70% enhancement of ultraslow electron emission compared to single-photon ionization. Another study employing momentum-resolved photoion detection¹⁶ concentrated on differences in photoion mass spectra and kinetic energy distributions for excitations above and below 24 eV. The results suggested that illumination of droplets with photon energies below 24 eV leads predominantly to surface excitations, while at higher energies electronically excited bulk states become accessible.

From a theoretical perspective, the groups of von Haeften and Head-Gordon have investigated the electronic structure of He droplets by ab initio methods for small clusters of 7 atoms^{13,14} and 25 atoms.¹⁴ While the electronic spectra for such small clusters have not been studied experimentally, ref 14 demonstrates remarkable agreement between the calculated lower band for He₂₅ and the experimental band²³ for He₃₀₀.

In this paper, the experimental method of ref 15 is employed using a Sn filter in the EUV pump beam to restrict excitation energies to less than 24 eV. The time-, energy-, and angular-resolved photoelectron imaging experiments exhibit clear differences compared to our previous work that was performed using a wider range of excitation energies extending beyond the atomic IP. The decay of the initially excited droplet state population and the emission dynamics of excited He atoms in 1s4p and 1s3d Rydberg states are observed in real-time. Based on the present observations as well as previous experimental^{8,23} and theoretical¹⁴ studies, a model is formulated that describes electronic excitations of He droplets in the framework of perturbed Rydberg states of

individual He atoms. This model supports the previous suggestions¹⁶ that excited states with energies below 24 eV are primarily located in the diffuse surface region of the droplet rather than within the droplet interior. The results of the modeling are in good agreement with experimental observations.^{7,11}

2. EXPERIMENTAL SECTION

The experimental setup is described in detail elsewhere.¹⁵ Briefly, helium droplets are produced by expanding 99.9999% pure helium gas through a 5 μ m diameter nozzle at a source temperature of 13 K and a source pressure of 80 bar, leading to the formation of droplets with an average size of 2×10^6 atoms.³ A beam of He atoms is obtained by switching off the cryogenic cooling and warming up the nozzle to temperatures above 100 K where condensation of He atoms to droplets becomes negligible.

Infrared (IR) light is produced by a two-stage amplified Ti:sapphire laser system (KMLabs Red Dragon), which generates 25 fs pulses (fwhm) with a central wavelength of 775 nm at a repetition rate of 3 kHz. The output is split by a wedged fused silica window into an intense transmitted beam (≈ 2 mJ pulse energy) that drives the high-order harmonic light source and a weaker probe beam with ≈ 1 μ J pulse energy at the interaction volume. The intense beam is focused into a gas cell filled with Kr at a stagnation pressure of 4 Torr to produce high-harmonic (HH) radiation. The EUV beam is reflected by a pair of Si mirrors that are positioned at Brewster's angle for 775 nm light, and passes through a thin metal filter. This setup removes the fundamental IR light used for the HH generation (HHG) from the EUV beam.²⁴

The time delay between the HH pump pulse and the IR probe pulse is controlled by routing the probe beam through a retro-reflector mounted on a computer-controlled linear translation stage. The probe beam is reflected by an annular mirror and recombined with the pump beam that passes through the center hole of the same mirror. Both beams are focused by a curved multilayer mirror and intersect the helium droplet beam in the center of a velocity map imaging (VMI) spectrometer. The multilayer mirror is optimized to reflect the 15th harmonic (24.5 ± 1.5 eV), but has non-negligible reflectance for higher order harmonics.

In the present work, a 200 nm thick Sn filter is used, which has a transmission window between 15.5 and 24 eV with a maximum transmission of 10%.²⁵ This photon energy range is much narrower than in our previous work,¹⁵ where a 100 nm thick Al filter transmitted HH light up to 38 eV. The resulting EUV spectrum of the pump pulse is centered at 23.6 eV before the multilayer mirror and has a full width at half-maximum (fwhm) of 0.4 eV.¹⁶ The upper limits for fluence of the pump- and probebeams in the interaction volume are estimated to 0.2 mJ/cm² and 250 mJ/cm², respectively. The full-width-at-half-maximum (fwhm) of the cross-correlation signal between the pump and probe pulses is 120 fs.

The polarization of the laser light is perpendicular to the VMI spectrometer axis. Photoelectrons are extracted using an electric field of about 1 kV/cm and imaged onto a detector that consists of two microchannel plates (MCPs) and a phosphor screen. This setup provides both kinetic energy spectra and angular distributions of the emitted electrons. The VMI images represent the Abel transform of the 3D velocity distributions of emitted electrons.²⁶ The original velocity distributions are recovered by carrying out an inverse Abel transformation. In this work a

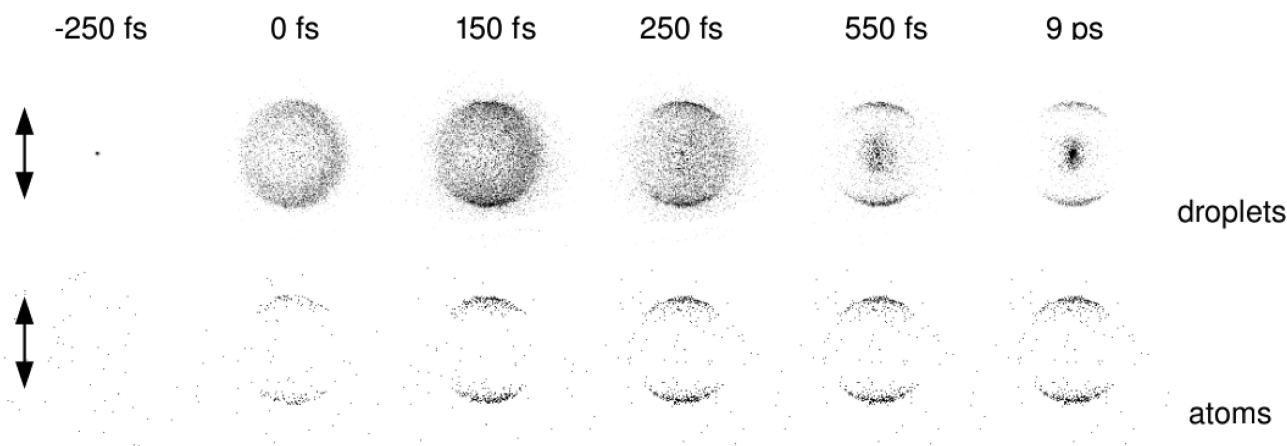


Figure 1. Photoelectron velocity map images for He droplets with $\langle N \rangle = 2 \times 10^6$ (top row) and He atoms (bottom row) for several pump–probe time delays. Differences between images for pump+probe and pump-only measurements are plotted, except for the images at the negative time delay of -250 fs, where pump-only images are shown. The white arrows indicate the polarization of the pump and probe pulses.

modified version of the BASEX method²⁷ is used to invert the images. The modification consists of replacing the Tikhonov regularization^{27,28} procedure with a non-negative minimum least-squares regression,²⁹ which insures that only non-negative distributions are produced. This procedure helps to reduce noise for images recorded over short integration times by applying the physical non-negativity constraint.

Data collection is performed by an automated data acquisition system that records VMI images with (“pump+probe”) and without (“pump-only”) the probe pulse for every time delay of a scan. The delay step width is 100 fs for scans spanning a range of 10 ps and 25 fs for scans spanning a range of 1 ps. For each measurement, the sequence of time steps is repeated several times in opposite scan directions to minimize the impact of long-term drifts in the experimental setup.

3. RESULTS

3.1. Overview. Figure 1 shows raw photoelectron images for He droplets (top row) and He atoms (bottom row) for several time delays between the EUV pump and the IR probe pulses. Photoelectrons at larger radii correspond to higher electron kinetic energy. The polarization of both the pump and probe pulses are vertical. The negative time-delay of -250 fs corresponds to a “pump-only” image, because the probe pulse does not interact with ground-state droplets or atoms. For positive time delays, the difference between the pump+probe signals and the pump-only signals is plotted, thus, the images comprise photoelectron signals resulting from ionization by the IR probe pulse of transient neutral excited states created by the pump pulse or, at later times, the decay products from these states.

The results for He atoms in Figure 1 are well-understood:³⁰ the EUV pump pulse excites the $1s4p$ Rydberg state at 23.74 eV, which is subsequently ionized by the IR probe pulse. The resulting photoelectron angular distributions (PADs) are strongly anisotropic.

The droplet data in Figure 1 exhibit more complex dynamics. At -250 fs, only a central point-like feature corresponding to near zero electron kinetic energy (ZEKE) electrons is observed, closely resembling the results of the synchrotron-based experiments.¹¹ At short time delays, photoelectron emission is

mainly concentrated in a broad isotropic ring, while the ZEKE signal is depleted. With increasing pump–probe delay, the intensity of the broad isotropic ring decreases, leaving a narrow anisotropic distribution at large radii similar to that observed for He atoms. For pump–probe delays beyond 500 fs, an anisotropic distribution appears at smaller radii, partly overlapping with the ZEKE peak. The ZEKE signal increases beyond its pump-only value for time delays beyond 500 fs. Hence, the images show that one droplet relaxation channel involves emission of $\text{He}^*(1s4p)$ Rydberg atoms, but there is also a lower energy electron signal that is not seen in the atomic images.

An inverse Abel transform of the raw VMI images followed by integration over all emission angles leads to the photoelectron energy distributions shown in Figure 2a as a function of pump–probe time delay. The distributions are plotted on a \sqrt{E} scale, which is proportional to the electron velocity, to make the slow electron features more visible. Figure 2b shows photoelectron spectra at selected time delays. The energy distribution at zero time delay is shown as a dark gray shaded area. The dashed curve represents the distribution at 0.2 ps delay. The kinetic energy distribution remains relatively unchanged for delay times longer than 5 ps. Hence, for improved statistics, the solid curve in Figure 2b is derived by averaging the spectra of Figure 2a from 5 to 9 ps. The light gray shaded area shows the kinetic energy distribution of photoelectrons produced by two-photon (EUV+IR) ionization of He atoms. All curves for He droplets are plotted on a common scale so that the intensities of features recorded at different time delays can be quantitatively compared. The curve for He atoms is scaled to match the solid curve at a kinetic energy of 0.76 eV.

In Figure 2b, the three main features of the spectrum are marked as “A”, “B”, and “ZEKE” for ease of reference. In the following, the dynamics of the three features are analyzed in detail. It is shown that feature A has two contributions: an anisotropic contribution with PADs similar to those of He atoms, which instantly rises and remains constant, and an isotropic contribution, which decays on a time scale of 220 fs. Feature B is characterized by a 200 fs rise time and has an anisotropic PAD. The ZEKE feature is depleted at zero time delay, but quickly recovers and continues growing over a time scale of 1.5 ps.

3.2. Dynamics of Feature A. Figure 2b shows that at zero time delay (dark gray), feature A is broad with a fwhm of 0.45 eV. At a

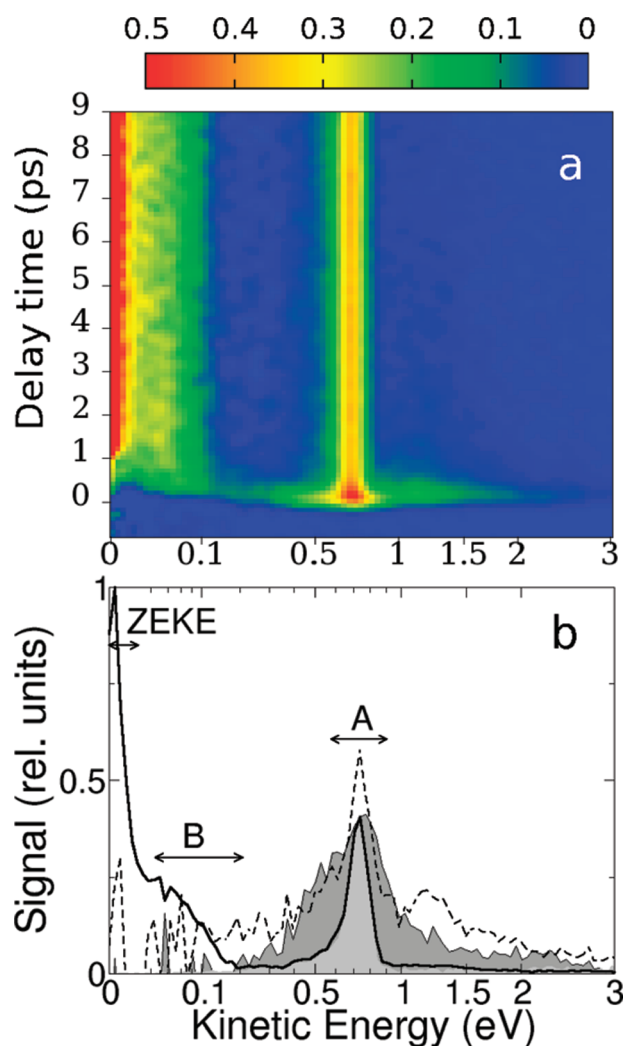


Figure 2. (a) Time-dependent kinetic energy distributions of photoelectrons plotted on a \sqrt{E} scale. (b) Photoelectron kinetic energy distributions at zero time delay (dark gray area), at 0.2 ps time delay (dashed) and at time delays longer than 5 ps (solid, averaged over 5–9 ps). The spectra are normalized to the maximum of the solid curve. The light gray shaded area shows a distribution for two-photon EUV+IR ionization of He atoms normalized to the maximum of feature A at 5 ps. Double arrows indicate energy ranges used in the analysis of transient behavior of features A, B, and ZEKE (see text).

small positive time delay of 0.2 ps (dashed), the spectrum in this region is more structured with a narrow (fwhm = 0.15 eV) peak at 0.76 eV on top of a broad pedestal that stretches over the entire spectrum and overlaps with feature B. For longer time delays beyond 4–5 ps, the broad part disappears, leaving only the narrow peak (solid line) that corresponds to ionization of the 1s4p Rydberg states of He atoms by the 1.6 eV probe pulse (light shaded area). Figure 2 shows that the kinetic energy distributions for delays below ≈ 1.5 ps extend to high kinetic energies beyond those observed for ionization of He atoms.

To obtain further insight into the dynamics of the electron signals contained in feature A, the associated PADs are analyzed. For improved statistics, the velocity maps are integrated over the energy range from 0.58 to 0.91 eV covering the maximum of feature A. This range is shown in

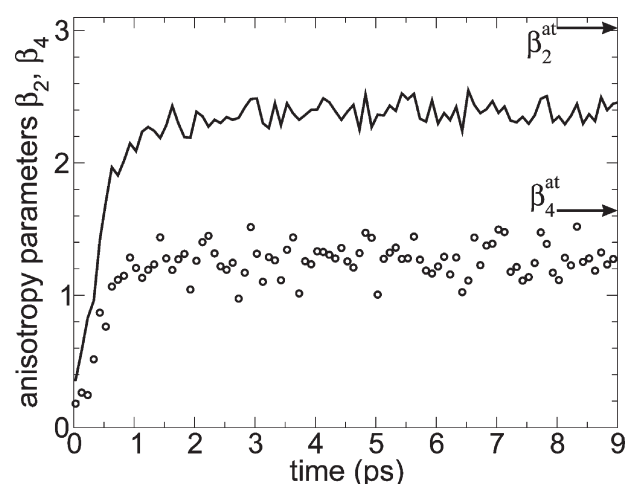


Figure 3. Time dependence of anisotropy parameters β_2 (solid) and β_4 (circles) for feature A. Arrows indicate experimentally determined values of anisotropy parameters $\beta_2^{\text{at}} = 3.02$ and $\beta_4^{\text{at}} = 1.64$ for ionization of He 1s4p Rydberg atoms with 800 nm radiation.³⁰

Figure 2b as a double arrow. For each pump–probe delay, the PAD of feature A is fit to the standard expression for two-photon ionization:^{31,32}

$$I = \frac{\sigma}{4\pi} (1 + \beta_2 P_2(\cos \theta) + \beta_4 P_4(\cos \theta)) \quad (1)$$

where σ is the relative ionization cross section, P_2 and P_4 are the Legendre polynomials of second and fourth order, respectively, and β_2 and β_4 are the anisotropy parameters of the PAD. In the least-squares fit, σ , β_2 , and β_4 are treated as free parameters. The resulting values of the anisotropy parameters β_2 and β_4 are plotted in Figure 3 as a function of the delay. At small delays, they are close to zero, corresponding to the isotropic emission shown in Figure 1 (0 fs). Both values increase over time, reaching their respective maxima of $\beta_2 = 2.4$ and $\beta_4 = 1.3$ by about 1.5 ps and remaining constant for longer time delays within the scatter of the data points.

Remarkably, the asymptotic ratio $\beta_2/\beta_4 = 1.85$ is equal to the ratio of the anisotropy parameters $\beta_2^{\text{at}} = 3.02$ and $\beta_4^{\text{at}} = 1.64$ for two-photon ionization of He atoms via the 1s4p state.³⁰ The evolution from an initially isotropic ($\beta_2 \approx \beta_4 \approx 0$) to an asymptotically anisotropic PAD marked by an atomic-like ratio of the anisotropy parameters can be modeled by describing feature A as a sum of two independent contributions with time-dependent intensities. The first contribution corresponds to photoemission from droplet excited states and is assumed to have an isotropic PAD. The second contribution corresponds to two-photon ionization of free He atoms. This sum is expressed as

$$I = \frac{\sigma^{\text{dr}}}{4\pi} + \frac{\sigma^{\text{at}}}{4\pi} (1 + \beta_2^{\text{at}} P_2(\cos \theta) + \beta_4^{\text{at}} P_4(\cos \theta)) \quad (2)$$

where σ^{dr} and σ^{at} are cross sections for two-photon ionization of droplets and atoms, respectively, and β_2^{at} and β_4^{at} are the atomic PAD anisotropy parameters.³⁰

Comparing the experimentally derived anisotropy parameters according to eq 1 with the PAD modeling according to eq 2, the intensities of the atomic and droplet contributions

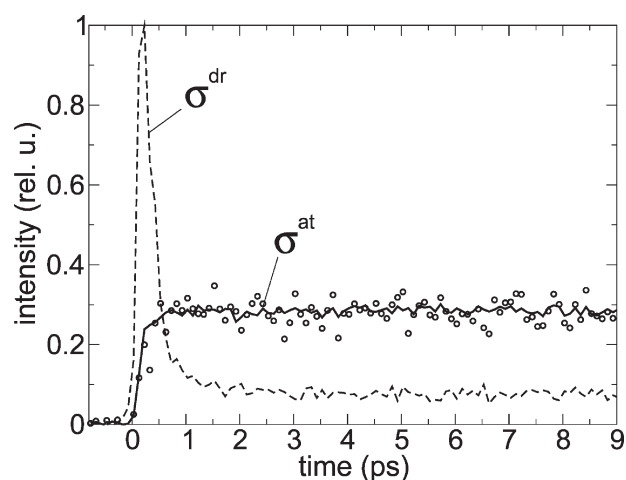


Figure 4. Time dependence of the atomic σ^{at} (solid line and circles) and droplet σ^{dr} (dashed) contributions to the signal of feature A. The partial cross sections $\sigma^{\text{at,dr}}$ are calculated by separating the time-dependent PADs of feature A into an isotropic (σ^{dr}) and an anisotropic (σ^{at}) component according to eq 3.

can then be obtained as

$$\sigma^{\text{at}} = \sigma \frac{\beta_2}{\beta_2^{\text{at}}} = \sigma \frac{\beta_4}{\beta_4^{\text{at}}} \quad \sigma^{\text{dr}} = \sigma - \sigma^{\text{at}} \quad (3)$$

Figure 4 shows the resulting temporal behavior of the two contributions. The isotropic part σ^{dr} rises instantly within the apparatus function and decays with a time constant of about 220 fs. These dynamics suggest that it is associated with the initially excited state of the He droplet. The atomic contribution σ^{at} appears within the time resolution of the experimental setup (120 fs) and remains constant for all positive time delays. According to eq 3, the atomic contribution can be calculated using either the β_2 or the β_4 anisotropy parameters. The results of both calculations are shown in Figure 4 as a solid line and as circles. The agreement between the two curves confirms that the ratio $\beta_2^{\text{at}}/\beta_4^{\text{at}}$ of the PAD of the feature A corresponds to the ratio β_2/β_4 of the PAD of atomic 1s4p ionization for all pump–probe time delays (eq 3). This supports the assumption that the anisotropic component of feature A originates from the ionization of orbitally aligned 1s4p atoms; the electronic alignment produced by the linearly polarized pump pulse is apparently retained.

3.3. Dynamics of Feature B. Feature B of Figure 2b appears at low photoelectron energies that approximately correspond to ionization of the 1s3p and 1s3d Rydberg states of He atoms. Its transient intensity is shown in Figure 5 after integration over the photoelectron kinetic energy range from 25 to 210 meV (indicated by the double arrow in Figure 2b). The signal quickly rises and remains constant for time delays up to 9 ps. The corresponding fit curve is shown in Figure 5 as a dashed line. A small depletion of the signal near zero time delay might be caused by the overlap between feature B and the tail of the ZEKE distribution; however, coherent artifacts can also influence this region and might cause the depletion. The rise time of feature B is about 200 fs, essentially the same as the 220 fs decay time of the isotropic part of feature A discussed in the previous section. This agreement suggests that feature B is a decay product of the transient droplet excited state associated with the isotropic component of feature A.

Transient angular anisotropy parameters of feature B are obtained using eq 1 and are plotted in Figure 6. Below 100 fs, the

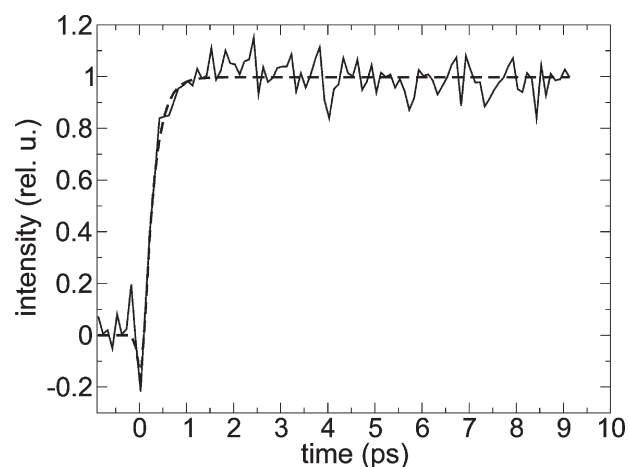


Figure 5. Time dependence of feature B (solid) and an exponential fit function (dashed).

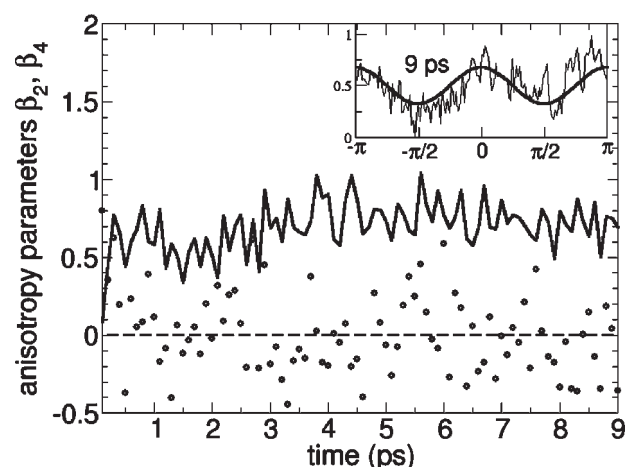


Figure 6. Time dependence of anisotropy parameters β_2 (solid) and β_4 (circles) for feature B. The inset shows the anisotropic PAD of feature B at 9 ps time delay with the corresponding fit to eq 1.

signal of feature B is too small to extract the anisotropy parameters reliably and, therefore, these data points are omitted from the plot. We find that β_4 is equal to zero for all delays within the scatter of the data points, while β_2 is essentially constant, with a value of about 0.75. A vanishing β_4 parameter occurs when the probe pulse ionizes an unaligned target, that is, the alignment of electronic orbitals that is induced in the excitation step is not apparent in the ionized products associated with feature B. To clarify the character of the relaxation products, the measured β_2 value is compared to theoretical predictions of PADs from unaligned 1s3p and 1s3d states of He atoms. Following Bethe, Cooper, and Zare,^{33,34} the anisotropy parameter β_2 can be expressed through the radial matrix elements and scattering phase shifts of the partial waves that describe the emitted photoelectron after ionization of atomic 1s3p or 1s3d states. The radial matrix elements and scattering phase shifts are calculated in the range of photon energies from 1.5 to 3.7 eV by numerical integration of the two-electron Schrödinger equation in a single active electron approximation. They are then used to calculate the anisotropy parameters β_2 and the results are plotted in Figure 7. For the current experiment, the

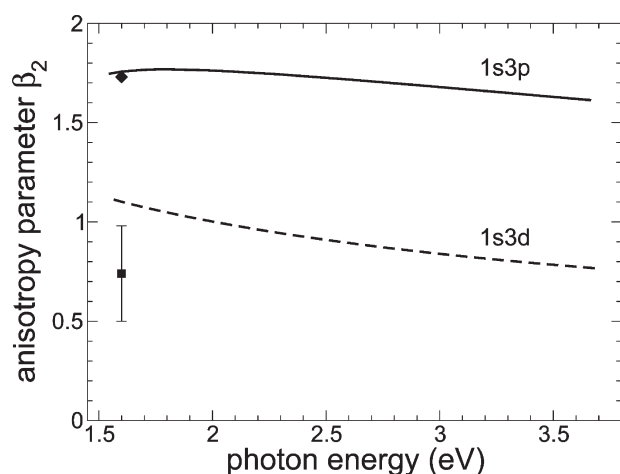


Figure 7. Photon energy dependence of the β_2 anisotropy parameter for one-photon ionization of unaligned 1s3p (solid) and 1s3d (dashed) Rydberg states of He atoms. The filled square shows the experimental value for He droplets (present work). The filled diamond shows the experimental value for the 1s3p state of He atoms.³⁰

values of interest are at the ionization photon energy of 1.6 eV (IR photon energy). The value for photoemission from unaligned 1s3p atoms can also directly be derived from the experimental results of ref 30. This value is shown in Figure 7 as a filled diamond and is in very good agreement with the calculation.

The experimentally observed value of $\beta_2 = 0.75$ is shown in Figure 7 as a filled square with the error bars determined from the scatter of points in Figure 6. The value is lower than both the anisotropy parameter for the 1s3d state, $\beta_2 = 1.1$, and for the 1s3p state, $\beta_2 = 1.75$. However, it is significantly closer to the value of the 1s3d state, suggesting that feature B originates predominantly from ionization of atoms emitted from He droplets in an unaligned 1s3d Rydberg state.

3.4. Dynamics of ZEKE Electrons. To probe the dynamics of the ZEKE electrons, the photoelectron distributions are integrated over the range of energies from 0 to 10 meV (shown by an arrow in Figure 2b) and over all emission angles. The resulting transient behavior is shown in Figure 8 as a ratio between the pump+probe and pump-only signals.

At zero time delay, when the pump and probe pulses overlap, the signal is reduced by about 15% compared to the pump-only intensity. It recovers by 200 fs and eventually overshoots the pump-only value by up to 45%. The transient can be well described by two exponentially rising components, while one exponentially rising component fails to describe the trend (see inset in Figure 8). The time constants of the two components are estimated to be about 200 fs and 1.5 ps, although the scatter of the data points limits the precision of this estimate to about $\pm 30\%$.

3.5. Comparison with Previous Measurements. The time-dependent photoelectron kinetic energy distributions of the present experiments have four distinct features. (i) The isotropic part of feature A decays on a time scale of 220 fs and is linked to the states initially excited by the EUV pulse. (ii) The anisotropic part of feature A rises very fast (within the experimental resolution) and remains constant for the whole range of scanned time delays (9 ps). The PAD of this channel is the same as that of free He atoms. (iii) Feature B has an anisotropic PAD and rises within 200 fs. (iv) The ZEKE signal is depleted at zero time delay, recovers in about 200 fs, and continues to rise with two time scales of 200 fs and 1.5 ps.

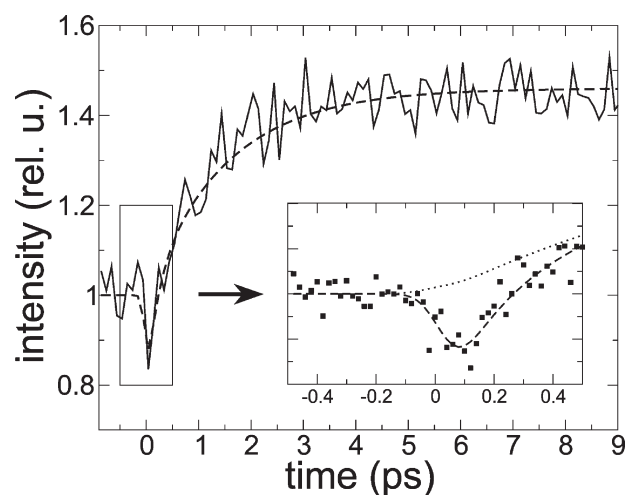


Figure 8. Time dependence of the ZEKE feature (solid) and a two-exponential fit function (dashed). The inset shows the result of a high resolution measurement in the vicinity of zero time delay. A one exponential fit function (dotted) fails to describe the depletion and recovery of the ZEKE signal.

The results of the present study differ from those previously reported with the same apparatus¹⁵ owing to the Sn filter used here, which resulted in a spectrally narrower pump pulse that is cut off above 24 eV. The PADs of the previous work also exhibited an energetically broad, isotropic component. The decay of this component, however, was accompanied by the emergence of two anisotropic rings, which were identified as contributions from ionization of 1s4p and 1s5p Rydberg states of He atoms. Under the conditions used here, the 1s5p state at 24.05 eV cannot be excited as illustrated by the atomic images in Figure 1.

The general shapes of the transients are similar in the two experiments, but the time scales are different. In the previous work, the decay of the broad isotropic distribution associated with initially excited droplet states was marked by two time scales on the order of 280 fs and 2.8 ps. Here, only the short time scale of 220 fs is observed.

A signal similar to that of feature B also appeared in the previous results, albeit it was much weaker than other observed contributions and its anisotropy or transient behavior could not be extracted reliably.

The dynamic trends of the ZEKE electron signal are similar in both experiments, but the extent of the signal variations and the time scales differ quantitatively. The magnitude of the overshoot in the previous study was 70% compared to 45% observed here. The rise time in both cases can be described by two time constants: 140 fs and 2.5 ps seen previously and 200 fs and 1.5 ps reported here. The difference between the fast time scales is not significant within the experimental uncertainty, but the difference between 1.5 and 2.5 ps is significant.

4. PERTURBED RYDBERG STATES MODEL OF He DROPLET EXCITATIONS

The differences between the dynamics recorded with different EUV filter materials must arise from the different pump pulse spectra used in the two experiments. The results of a recent femtosecond EUV-pump IR-probe photoion imaging study have been interpreted as an indication that, within the electronic band

centered around 23.8 eV, excitation below 24 eV leads predominantly to surface states while excitations above this value may also access bulk states.¹⁶ In this section, a simple model is formulated that quantitatively supports this assertion based on a description of excited droplet states in terms of atomic Rydberg states perturbed by the He droplet environment.

The model is based on a single-electron picture of an excitation localized on one He atom and a mean-field effect of other He atoms surrounding it. The excited atom is assumed to be in a spherical cavity with a radius r_{nn} equal to a distance to the nearest neighboring atom in the droplet. This approach is in many respects similar to the one taken by Dobrosavljevic et al. to describe the electronic structure of molecules dissolved in a hard-sphere liquid.³⁵ The r_{nn} distribution is peaked at about 3 Å in neutral helium clusters.¹² The potential for a Rydberg electron is modeled by the sum of the Coulomb potential of a hydrogen-like ion and a repulsive potential, which represents the effect of the surrounding He atoms:

$$V = -\frac{1}{r} + V_0(\vec{r}, R)\Theta(r - r_{nn}) \quad (4)$$

where \vec{r} is the radius vector of the electron referenced to the ion, $\Theta(r)$ is the Heaviside step function, and $V_0(\vec{r}, R)$ is the effective repulsive potential imposed by the droplet environment for the excitation located at a distance R from the center of the droplet. The presence of the ion is assumed to have no influence on the interaction between the electron and the surrounding neutral He atoms, effectively leading to an approximation of the potential V_0 by that of a free electron in liquid He. The latter has been previously determined to ≈ 1 eV (0.037 au) in bulk helium,^{36,37} and indications for a similar potential in helium nanodroplets have been recorded.³⁸ Different local densities ρ in the surface region of the droplet are modeled by varying the value of V_0 between 0.037 au (bulk limit) and 0 (free atom limit): $V_0(\vec{r}, R) = 0.037 \times (\rho(\vec{r}, R)/\rho_{\text{bulk}})$, where $\rho_{\text{bulk}} = 22 \text{ nm}^{-3}$. Experiments at variable densities of liquid He support this linear scaling.³⁷ Thus, taking into account the expression for the droplet density profile of Harms et al.,³⁹ the repulsive potential is expressed as

$$V_0(\vec{r}, R) = 0.037 \times \frac{1}{2} \left(1 - \tanh \left(2 \frac{r \cos \theta + R - R_0}{\gamma} \right) \right) \quad (5)$$

where θ is the angle between the vectors \vec{r} and \vec{R} , R_0 is the radius of the droplet, and $\gamma \approx 5$ Å is the parameter defining the thickness of the droplet surface region.³⁹ The dependence on θ in eq 5 reflects the fact that near the surface the droplet density is anisotropic. A section of the model potential is shown in the inset of Figure 9.

The Schrödinger equation is solved by diagonalizing the model Hamiltonian within a basis of hydrogenic Rydberg states. We approximate the helium Rydberg wave functions by hydrogen wave functions, but use the literature values for their energies.⁴⁰ The cylindrically symmetric repulsive part of the potential lifts the degeneracy of the levels within Rydberg state manifolds with the same principal quantum number n and mixes states with different orbital quantum numbers l , but the same magnetic quantum number m . In the vicinity of the droplet surface, the $n = 3$ manifold is split into 6 levels and the $n = 4$ manifold is split into 10 levels. In the bulk, where the density is approximately constant, the problem is spherically symmetric and the splitting reduces to 3 and 4 levels, respectively.

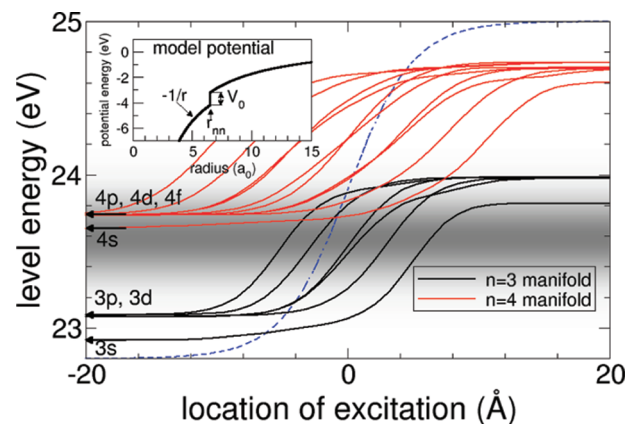


Figure 9. Energies of perturbed Rydberg state manifolds for the principal quantum numbers $n = 3$ (black) and $n = 4$ (red) calculated for the value $r_{nn} = 3$ Å. The gray band indicates the spectral intensity profile of the EUV pulse centered at 23.6 eV. The black arrows mark positions of the $n = 3$ and $n = 4$ levels of isolated He atoms. The dashed blue curve is the helium droplet density profile plotted for comparison. The inset shows the shape of the model potential used in the calculations.

Energies of perturbed $n = 3$ and $n = 4$ states are plotted in Figure 9 as functions of the location of the excitation with respect to the droplet surface. The zero of the abscissa corresponds to the position of the equimolar surface. This surface is defined as the boundary of a virtual hard sphere with a uniform density equal to the droplet bulk density, which contains the same total number of atoms as the droplet. For helium droplets,³⁹ it closely corresponds to the radius, at which the local density is 50% of the bulk value.

The blue-shifts that result from this model for Rydberg states in the bulk limit are on the order of the maximum repulsive potential of 1 eV. In the surface region, the energy of the $n = 4$ states changes from 23.74 (unperturbed) to 24.7 eV (bulk limit). The pump photon energy shown by the gray shaded band restricts excitation within the $n = 4$ Ry manifold to very weakly perturbed atoms. The $n = 3$ manifold changes in energy from 23.09 eV at zero density to almost 24 eV in the bulk limit. The spectral range containing 90% of the pump pulse energy leads to excitations of the $n = 3$ band in the surface region, where the local density varies between 10 and 85% of the bulk density. The radial range, where the excitation predominantly localizes, is estimated to extend from -7 to $+5$ Å relative to the equimolar surface. Thus, the photon energy is mostly insufficient to excite the perturbed Rydberg states of this band within the droplet interior, which supports the assertion that below 24 eV the excitation is predominantly localized in the surface region of the droplet.

Using this model, one can calculate the absorption bands of He droplets arising from Rydberg states of the $n = 2-4$ manifolds. It is assumed that the excitation is localized on a random atom in the droplet. For each possible location, the energy of the perturbed Rydberg state depends on the parameters of the model: the nearest-neighbor distance r_{nn} and the local density ρ . Because droplets are liquid and have a diffuse surface, these parameters vary for different locations. The local environment of excited atoms is modeled taking into account the following properties of He droplets:

- Local densities ρ depend on density profiles of He droplets, which in turn depend on the droplet size. Here the profiles are modeled according to the measurements of Harms and co-workers³⁹ and a log-normal droplet size distribution is applied

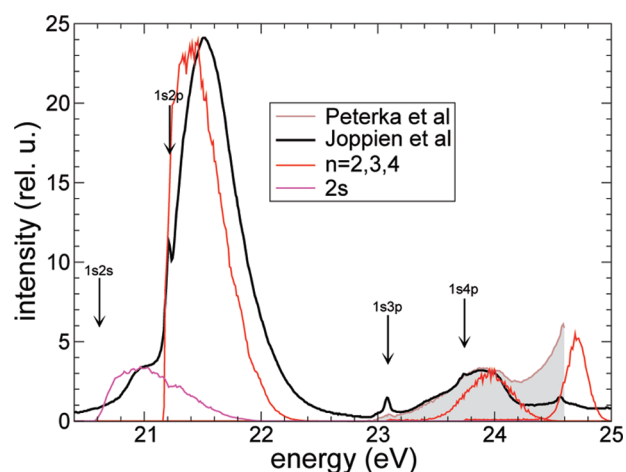


Figure 10. Comparison of fluorescence excitation spectrum⁷ (solid, black) and total photoelectron yield¹¹ (shaded area) with excitation bands based on perturbed 1s2s (magenta), 1s2p, $n = 3$, and $n = 4$ (all red) Rydberg states. The intensities of the bands are arbitrarily scaled to aid comparison. Arrows mark the positions of atomic excitation energies.

with a mean value of 2×10^6 atoms^{3,41} per droplet. The width of the log-normal distribution is taken to be maximal.⁴²

- (ii) The radius of the cavity r_{nn} is approximated by the nearest-neighbor distribution calculated by Peterka et al.¹² with a mean value of 3 Å and fwhm of about 1 Å. The use of the nearest-neighbor distribution provides an upper bound on the perturbed Rydberg state energies.
- (iii) Rydberg electrons experience repulsive interaction not uniformly, but in a number of localized spots, where surrounding He atoms are located. This means that variations of local density outside of the cavity (i.e., variations of the number of involved atoms) results in proportional variations of the repulsive potential V_0 . These variations lead to a large inhomogeneous broadening of the excitation bands and are taken into account in the calculation. An estimate of the local density variations is given in the Appendix.

The resulting absorption spectrum is shown in Figure 10 and is compared to the fluorescence excitation spectrum of Joppien and co-workers⁷ and the total electron yield spectrum of Peterka et al.,¹¹ both recorded with $\langle N \rangle = 10^4$ atom clusters. Joppien et al. also published a spectrum for 10^6 atom clusters but pointed out that it is distorted by saturation effects and suggested that the spectrum for 10^4 atom clusters is a better approximation for absorption in large droplets and bulk He. The current level of calculations does not provide information on relative oscillator strengths of the electronic states. Therefore, all bands are arbitrarily scaled to aid comparison with the experimental data.

The overall agreement between the calculated and the measured absorption spectra in Figure 10 is remarkable. The model reproduces the position of the 1s2s band and the major portion of the 1s2p band. The maximum position and the high energy slope of the upper band at 23.8 eV are well reproduced, too.

5. DISCUSSION

The analysis of section 4 indicates that, under the conditions of this experiment, at an excitation energy of 23.6 eV with a fwhm of 0.4 eV, electronic excitation of the droplet occurs primarily in

the diffuse surface region of the droplet. As shown in Figure 9, the excitation of the $n = 4$ band mostly occurs in the outer regions away from the equimolar surface, where the states are weakly perturbed. The more strongly perturbed $n = 3$ band is excited deeper in the droplet surface region. This picture can be used to explain many aspects of our results, as it appears that relaxation pathways depend on the location of the initial excitation with respect to the surface of the droplet.

We first consider the anisotropic contribution of feature A, which corresponds to photoionization of aligned 1s4p Rydberg atoms. From Figure 4, this signal appears faster than the time resolution of the current experiment. The fast appearance time and the preservation of orbital alignment suggest that this contribution originates from atoms excited at the outer surface layer of He droplets, which have nearly unperturbed Rydberg states energies of the $n = 4$ manifold. The only states, which would be excited in this case are the 1s4p states, which have prevailing oscillator strength. The emission of these atoms proceeds on a sub-100 fs time scale and the interaction with the droplet is not sufficient to modify the alignment of the electronic orbital induced by the excitation pulse. Experiments with improved time resolution are required to identify the relevant rates of emission of these Rydberg atoms. We note that major contributions to the 1s4p pump–probe signal from residual atomic helium gas are ruled out by the results of a complementary ion imaging study; a corresponding manuscript is currently in preparation.

The instant rise of the isotropic component of feature A at zero time delay suggests that it arises from IR ionization of states initially populated by the EUV pulse (dark gray area in Figure 2b). Its fwhm of 0.45 eV roughly corresponds to that of a convolution of the pump (0.4 eV) and probe (0.15 eV) pulses. This signal decays with a time constant of 220 fs. Based on the results of Figure 9, this component is assigned to excitation of the surface part of the band emerging from perturbed $n = 3$ Rydberg states. This picture is consistent with the isotropic PAD of this component because photoelectrons emerging from the (inner) surface region of the droplet are expected to be subject to significant scattering on surrounding helium atoms.

The ≈ 200 fs rise time of feature B in Figure 5 is consistent with the ≈ 220 fs decay time of the isotropic part of feature A. Feature B is energetically compatible with the ionization of either the 1s3p or the 1s3d Rydberg state of He* atoms. The analysis in section 3.3 attributes feature B primarily to unaligned He*(1s3d) atoms based on the PAD of this feature. Hence, it appears that these atoms are a decay product of the droplet states that emerge from perturbed atomic $n = 3$ Rydberg states and that are responsible for the isotropic component of feature A.

Our assignment is consistent with the spectrally resolved fluorescence measurements of von Haeften et al. who found that the most intense signals are associated with 1s3d \rightarrow 1s2p transitions subsequent to droplet excitation at 23.1 eV. It is likely that, in both experiments, excitation of droplet states that emerge from the atomic $n = 3$ manifold leads predominantly to ejection of 1s3d Rydberg atoms with no obvious electronic alignment in the laboratory frame. These dynamics would have to occur within ≈ 200 fs of the excitation pulse. Note that the radiative life times of atomic helium Rydberg states with principal quantum numbers $n = 3, 4$ are on the order of 1.7–3.9 ns and, therefore, have no impact on the subpicosecond dynamics discussed here.^{43,44}

While the droplet excited state can also decay via emission of He*(1s3s), this state has an energy of 22.920 eV and cannot be ionized by the IR pulse in our experiment. However, the previous

fluorescence study⁸ showed relatively little signal from transitions involving the 1s3s state.

The analysis in section 4 also provides a rationalization for the differing results here compared to ref 15, as summarized in section 3.5. The higher photon energy range in that work not only accesses states at the droplet surface that decay by prompt ejection of He*(1s5p), but can also excite $n = 4$ and $n = 3$ states deeper within the droplet. Hence, for example, the longer decay of 2.8 ps seen in ref 15, but not in the current study, most likely reflects the differing electronic character of the initially excited states in the two experiments.

The interband relaxation channel discussed in ref 15 is also observed for the excitation regime of the present experiment via dynamics of the ultraslow ZEKE electrons shown in Figure 8. It is described by a re-excitation picture, in which the probe pulse transfers population from the lower band back into the upper band. This mechanism results in an additional production of ultraslow electrons leading to the overshoot in Figure 8 (correspondingly, in Figure 6a of ref 15). In agreement with the previous results, the ZEKE signal in the present experiment overshoots its pump-only intensity at large delays. Because the overshoot constitutes up to 45%, significant population must relax to the lower electronic band in the vicinity of 21.6 eV.

The present and the previously published results differ in the magnitude of the overshoot and the time constants of the transients. While in the case of the Al filter measurements a 70% overshoot of the ZEKE signal was observed, here the overshoot is only 45%. The rise time of the overshoot is 1.5 ps compared to the 2.5 ps reported earlier. A shorter relaxation time and a smaller population of the lower band in the present experiment (expressed in the magnitude of ZEKE overshoot) suggest competition of bulk and surface relaxation channels.

6. CONCLUSIONS

Time-resolved pump–probe photoionization experiments of large He droplets are carried out using a femtosecond HHG-based light source. The EUV pump spectrum is filtered by a Sn filter to limit the excitation energies to less than 24 eV. Experimental results demonstrate relaxation of the initial excitation on a time scale of 220 fs, leading either to emission of unaligned 1s3d Rydberg atoms or to states at the bottom of the upper droplet band that subsequently decay via interband relaxation to the lower electronic band. Aligned 1s4p Rydberg atoms emerge within the time resolution of the experiment (120 fs). Enhanced emission of ultraslow electrons is observed similar to previous experiments,¹⁵ albeit at a shorter time scale of 1.5 ps.

Based on a model of perturbed atomic Rydberg states, excitation below 24 eV is proposed to be predominantly localized in the surface region of the He droplet. It is suggested that the relaxation dynamics depend on the position of the initial excitation. Atoms excited in the outermost region of the droplet are relatively unperturbed by the droplet and are emitted in an aligned 1s4p Rydberg state. Excitations localized deeper in the droplet surface lead partially to emission of the unaligned 1s3d Rydberg states and partially to interband relaxation or emission of ultraslow ZEKE electrons. The results of the modeling suggest that, at photon energies above 24 eV,¹⁵ excitations are preferentially localized in the bulk of He droplets leading to different relaxation dynamics. The model of perturbed atomic Rydberg states is used to simulate the absorption spectrum of the droplet. The results are in remarkable agreement with experimental

observations^{7,11} and suggest that a large fraction of the upper excitation band of He droplets can be assigned to a combination of perturbed atomic $n = 3$ and $n = 4$ Rydberg manifolds. The achievements of this simple model are encouraging for an extended modeling of the electronic structure and dynamics of He droplets on the basis of perturbed Rydberg states. We expect that the inclusion of anisotropy effects and hole delocalization will capture details of the experimental results that are currently not included in the theoretical description. The concept of distinguishing surface and bulk excitations in pure helium droplets has very recently been discussed in the work of von Haeften and co-workers.⁹

APPENDIX

Local density fluctuations can be estimated using a model, which represents interaction of the Rydberg electron with neutral atoms as delta-functions. Assume that the Rydberg electron is described by a spatially localized normalized wave function $\Psi(r)$, which is fully contained in a large volume Ω . Further assume that the volume Ω contains N randomly distributed He atoms such that $N/\Omega = \rho$, the local density. A part of potential energy of the Rydberg electron, related to repulsive interaction with He atoms, can be expressed via a sum of individual potentials:

$$V = \alpha \sum_N |\Psi(r_N)|^2 \quad (6)$$

where r_N are positions of the He atoms and α is the coefficient of proportionality between the repulsive contribution of one atom and the electron density. If positions of all He atoms are completely random and uncorrelated, then the value of the repulsive potential averaged over all possible configurations of He atoms is expressed via the N -fold integral of the Rydberg electron wave function

$$\langle V \rangle = \alpha \sum_N \frac{1}{\Omega} = \alpha \frac{N}{\Omega} = \alpha \rho \quad (7)$$

Since the average potential in the bulk He is equal to 1 eV, $\alpha = 1 \text{ eV}/\rho_{\text{bulk}}$.

The variation of the local density can be calculated by using the conventional formula for dispersion $D(V)$ of a random variable V :

$$D(V) = \langle V^2 \rangle - \langle V \rangle^2 \quad (8)$$

where $\langle \cdot \rangle$ means averaging over random uncorrelated positions of all He atoms. Using the definition of the repulsive potential, the dispersion is expressed as

$$\begin{aligned} D(V) &= \langle V^2 \rangle - \langle V \rangle^2 = \alpha^2 \left\langle \left(\sum_N |\Psi(r_N)|^2 \right)^2 \right\rangle - \alpha^2 \rho^2 \\ &= \alpha^2 \sum_{N,M} \langle |\Psi(r_N)|^2 |\Psi(r_M)|^2 \rangle - \alpha^2 \rho^2 \\ &= \alpha^2 \left(\sum_{N \neq M} \frac{1}{\Omega^2} + \sum_N \langle |\Psi(r_N)|^4 \rangle - \rho^2 \right) \\ &= \alpha^2 \left(\frac{N(N-1)}{\Omega^2} + \frac{N}{\Omega} \int |\Psi(r)|^4 dr - \rho^2 \right) \\ &\approx \alpha^2 \rho \int |\Psi(r)|^4 dr \quad (9) \end{aligned}$$

The last equality is essentially exact if the infinite volume Ω is taken.

Therefore, the variation of the local density can be expressed via the integral of the fourth power of the wave function. In the calculation of the absorption bands, the variation of the local repulsive potential is approximated by a Gaussian distribution with the dispersion $D(V)$.

AUTHOR INFORMATION

Corresponding Author

*E-mail: kornilov@mbi-berlin.de.

Present Addresses

^SMax-Born-Institute, Max-Born-Str. 2A, 12489 Berlin, Germany

^{||}Institute for Physical Chemistry, Georg-August-University Göttingen, Tammanstr. 6, 37077 Göttingen, Germany

ACKNOWLEDGMENT

O.B. would like to thank the Deutsche Forschungsgemeinschaft for funding his tenure at the Ultrafast X-ray Science Laboratory. This work was supported by the Director, Office of Science, Office of Basic Energy Sciences, Chemical Sciences Division of the U.S. Department of Energy under Contract No. DE-AC02-05CH11231.

REFERENCES

- (1) Hartmann, M.; Miller, R. E.; Toennies, J. P.; Vilesov, A. *Phys. Rev. Lett.* **1995**, *75*, 1566.
- (2) Grebenev, S.; Toennies, J. P.; Vilesov, A. F. *Science* **1998**, *279*, 2083.
- (3) Toennies, J. P.; Vilesov, A. F. *Angew. Chem., Int. Ed.* **2004**, *43*, 2622.
- (4) Stienkemeier, F.; Vilesov, A. F. *J. Chem. Phys.* **2001**, *115*, 10119.
- (5) Mozhayanskiy, V.; Slipchenko, M. N.; Adamchuk, V. K.; Vilesov, A. F. *J. Chem. Phys.* **2007**, *127*, 094701.
- (6) Nauta, K.; Miller, R. E. *Science* **1999**, *283*, 1895.
- (7) Joppien, M.; Karnbach, R.; Möller, T. *Phys. Rev. Lett.* **1993**, *71*, 2654.
- (8) von Haeften, K.; de Castro, A. R. B.; Joppien, M.; Moussavizadeh, L.; von Pietrowski, R.; Möller, T. *Phys. Rev. Lett.* **1997**, *78*, 4371.
- (9) von Haeften, K.; Laarmann, T.; Wabnitz, H.; Möller, T.; Fink, K. *J. Phys. Chem. A* **2011**, DOI: 10.1021/jp2008489
- (10) Frochtenicht, R.; Henne, U.; Toennies, J. P.; Ding, A.; Fieber-Erdmann, M.; Drewello, T. *J. Chem. Phys.* **1996**, *104*, 2548.
- (11) Peterka, D. S.; Lindinger, A.; Poisson, L.; Ahmed, M.; Neumark, D. M. *Phys. Rev. Lett.* **2003**, *91*, 043401.
- (12) Peterka, D. S.; Kim, J. H.; Wang, C. C.; Poisson, L.; Neumark, D. M. *J. Phys. Chem. A* **2007**, *111*, 7449.
- (13) von Haeften, K.; Fink, K. *Eur. Phys. J. D* **2007**, *43*, 121.
- (14) Closser, K. D.; Head-Gordon, M. *J. Phys. Chem. A* **2010**, *114*, 8023.
- (15) Kornilov, O.; Wang, C. C.; Bünermann, O.; Healy, A. T.; Leonard, M.; Peng, C.; Leone, S. R.; Neumark, D. M.; Gessner, O. *J. Phys. Chem. A* **2010**, *114*, 6350.
- (16) Bünermann, O.; Kornilov, O.; Leone, S. R.; Neumark, D. M.; Gessner, O. *J. Sel. Topics Quantum Electron.* **2011**, DOI: 10.1109/JSTQE.2011.2109054 (published online Apr 7, 2011).
- (17) Neumark, D. M. *Annu. Rev. Phys. Chem.* **2001**, *52*, 255.
- (18) Stolow, A.; Underwood, J. G. *Adv. Chem. Phys.* **2008**, *139*, 497.
- (19) Suzuki, T.; Whitaker, B. J. *Imaging in Molecular Dynamics*; Cambridge University Press: Cambridge, U.K., 2003.
- (20) Li, X. F.; L'Huillier, A.; Ferray, M.; Lompré, L. A.; Mainfray, G. *Phys. Rev. A* **1989**, *39*, 5751.
- (21) Zhou, J.; Peatross, J.; Murnane, M. M.; Kapteyn, H. C.; Christov, I. P. *Phys. Rev. Lett.* **1996**, *76*, 752.

- (22) Pfeifer, T.; Spielmann, C.; Gerber, G. *Rep. Prog. Phys.* **2006**, *69*, 443.
- (23) von Haeften, K.; Laarmann, T.; Wabnitz, H.; Möller, T. *Phys. Rev. Lett.* **2001**, *87*, 153403.
- (24) Takahashi, E.; Nabekawa, Y.; Nurhuda, M.; Midorikawa, K. *J. Opt. Soc. Am. B* **2003**, *20*, 158.
- (25) Henke, B. L.; Gullikson, E. M.; Davis, J. C. *At. Data Nucl. Data Tables* **1993**, *54*, 181.
- (26) Eppink, A. T. J. B.; Parker, D. H. *Rev. Sci. Instrum.* **1997**, *68*, 3477.
- (27) Dribinski, V.; Ossadtchi, A.; Mandelshtam, V. A.; Reisler, H. *Rev. Sci. Instrum.* **2002**, *73*, 2634.
- (28) Tikhonov, A. *Dokl. Akad. Nauk SSSR* **1963**, *151*, 501.
- (29) Bro, R.; De Jong, S. J. *Chemom.* **1997**, *11*, 393.
- (30) Haber, L. H.; Doughty, B.; Leone, S. R. *Phys. Rev. A* **2009**, *79*, 031401.
- (31) Tully, J. C.; Berry, R. S.; Dalton, B. J. *Phys. Rev.* **1968**, *176*, 95.
- (32) Reid, K. *Annu. Rev. Phys. Chem.* **2003**, *54*, 397.
- (33) (a) Cooper, J.; Zare, R. N. *J. Chem. Phys.* **1968**, *48*, 942.
- (b) Cooper, J.; Zare, R. N. *J. Chem. Phys.* **1968**, *49*, 4252.
- (34) Bethe, H.; Salpeter, E. E. *Quantum Mechanics of One- and Two-Electron Atoms*; Academic Press, New York, 1957.
- (35) Dobrosavljevic, V.; Henebry, C. W.; Stratt, R. M. *J. Chem. Phys.* **1988**, *88*, 5781–5789.
- (36) Sommer, W. T. *Phys. Rev. Lett.* **1964**, *12*, 271.
- (37) Broomall, J. R.; Johnson, W. D.; Onn, D. G. *Phys. Rev. B* **1976**, *14*, 2819.
- (38) Wang, C. C.; Kornilov, O.; Gessner, O.; Kim, J. H.; Peterka, D. S.; Neumark, D. M. *J. Phys. Chem. A* **2008**, *112*, 9356.
- (39) Harms, J.; Toennies, J. P.; Dalfvo, F. *Phys. Rev. B* **1998**, *58*, 3341.
- (40) Ralchenko, Y.; Kramida, A.; Reader, J.; NIST ASD Team *NIST Atomic Spectra Database*; National Institute of Standards and Technology: Gaithersburg, MD, **2010**, accessed online June 2, 2011; <http://physics.nist.gov/asd3>.
- (41) Lewerenz, M.; Schilling, B.; Toennies, J. P. *Chem. Phys. Lett.* **1993**, *206*, 381.
- (42) Kornilov, O.; Toennies, J. *Int. J. Mass Spectrom.* **2009**, *280*, 209.
- (43) Johansson, A.; Raarup, M.; Li, Z.; Lokhnygin, V.; Descamps, D.; Lyngå, C.; Mevel, E.; Larsson, J.; Wahlström, C.-G.; Aloise, S.; Gisselbrecht, M.; Meyer, M.; L'Huillier, A. *Eur. Phys. J. D* **2003**, *22*, 3.
- (44) Theodosiou, C. E. *At. Data Nucl. Data Tables* **1987**, *36*, 97.

EDITOR'S COMMENTS

[†]Originally submitted for the “J. Peter Toennies Festschrift”, published as the June 30, 2011, issue of *J. Phys. Chem. A* (Vol. 115, No. 25).